Beach-ridge formation as a possible indicator for an open Limfjord – North Sea connection

Trine H. Freiesleben*[1,2] , Lasse R. Berntsen[1] , Maria Blæsbjerg[1] , Emilia Høffer[1] , Christian F. Rasmussen[3,4] and Nicolaj K. Larsen[5]

[1]Department of Natural Science (INM), Roskilde University, Roskilde, Denmark; [2]Department of Physics, Technical University of Denmark, DTU Risø Campus, Roskilde, Denmark; [3]UNESCO Global Geopark, Vestjylland, Denmark; [4]Department of Ecoscience, Aarhus University, Aarhus, Denmark; [5]Globe Institute, University of Copenhagen, Copenhagen, Denmark

Abstract

Raised beach ridges are prograded sequences of wave-built deposits that may provide valuable information about past relative sea-level changes, climate change and coastal evolution. In the Limfjord in northern Denmark, the Early and Middle Holocene sea-level changes are well-constrained. However, our understanding of Late Holocene sea-level fluctuations is limited, and the exact period when the coastal barrier between the Limfjord and the North Sea formed remains uncertain. In this study, we use optically stimulated luminescence (OSL) dating to determine the age of raised beach ridges at Gjellerodde in the western part of the Limfjord. The OSL ages presented here indicate that the beach ridges formed during three periods at 3.3–2.7, 1.4–1.0, 0.2–0.1 ka. In addition our data suggest a c. 0.2 mm/yr relative sea-level fall during the Late Holocene. The three distinct periods of beach-ridge formation coincide with periods when the Limfjord was open towards the North Sea as documented in historical records and marine records. This suggests that OSL dating of beach ridges can be used as a potential indicator for determining when the connection between the Limfjord and the North Sea was open in the Late Holocene.

1. Introduction

Humans and habitats in coastal regions are vulnerable to sea-level changes, coastal erosion and climate change that may impact protected fjord environments by opening or closing coastal barriers to the open sea (Goodwin *et al*. 2006; Sander *et al*. 2016). Exploring how fjord environments have adapted to natural climate shifts may provide valuable information about how it may evolve in the future as a response to global climate change with rising sea levels and severe storms (Shukla *et al*. 2022).

The Limfjord in northern Denmark is an estuary that is presently connected to the North Sea in the west by an artificially maintained channel (Thyborøn Kanal) dividing the coastal barrier called Harboøre Tange (south) and Agger Tange (north) which are collectively referred to as Limfjordstangerne (Fig. 1). Since the last deglaciation, the Limfjord has experienced repeated paleoenvironmental changes because of the intricate interplay between glacio-isotatic uplift and eustatic sea-level changes as well as the development and destruction of coastal barriers (Bennike *et al*. 2019). The postglacial sea-level history in the Limfjord area is based on radiocarbon dating of terrestrial-to-marine transitions in sediment cores, and mollusc shells in raised marine deposits showing a rapid sea-level rise in the Early Holocene (Petersen 1979; Bennike *et al*. 2019; Jessen *et al*. 2019) followed by a Middle Holocene peak in sea level 2–5 m higher than present as documented by the raised beach ridges and Littorina shorelines (Mertz 1924). In the Middle Holocene during the Littorina Sea stage (Penney 1985), large

Abbreviations:
a.s.l.: above sea level
BP: before present (i.e. before 1950)
CE: common era
DEM: digital elevation model
$\dot{D}$: environmental dose rate
$\dot{D}_e$: equivalent dose
DRC: dose response curve
HF: hydrofluoric
IR: infrared
IRSL: infrared stimulated luminescence
IQR: inter quartile rejection
ka: thousand years
OSL: optically stimulated luminescence
pIRIR: post-IR IRSL
PTTL: photo-transferred TL
RSE: relative standard error
RSL: relative sea level
SAR: single-aliquot regenerative dose
TL: thermoluminescence
w.c.: water content

wide connections existed between the Limfjord and the North Sea, Skagerrak and Kattegat (Jessen 1910). These connections became shallower or were completely closed by a combination of long-shore sediment transport and continued glacio-isostatic uplift that outpaced the eustatic sea-level rise in the Late Holocene.

The closing of the gateways resulted in lower salinity and brackish conditions in the Limfjord. However, when the gateways shrank they also became sensitive to the development and destruction of coastal barriers between the Limfjord and the North Sea. This interplay between sea-level changes and coastal processes led to several periods with fully marine conditions when the natural gateways to the west were open, interrupted by periods of more brackish water when the connections were closed (Kristensen *et al*. 1995; Lewis *et al*. 2013). Both the relative sea-level (RSL) changes and physical properties of the Limfjord are well-constrained in the Early and Middle Holcoene (Bennike *et al*. 2019; Jessen *et al*. 2019; Kristiansen *et al*. 2021). However, less is known about the Late Holocene RSL and their influence on the development of the Limfjord. In particular, it is uncertain when the Limfjordstangerne became established and created a barrier toward the North Sea and how stable this barier was in the last 2000–3000 years (Kristiansen *et al*. 2021). Historical documents show that the Limfjord was separated from the North Sea by a coastal barrier (Limfjordstangerne) for an extended time prior to 1825 CE and it was only interrupted by short periods with open passage (Gram-Jensen 1991).

Raised beach ridges constitute a sedimentary archive that can be used to reconstruct Holocene sea-level changes, coastal evolution and climate changes (c.f. Sander *et al*. 2016). This method has successfully been used to reconstruct the Middle and Late Holocene in numerous places around the world, including Denmark (Tamura *et al*. 2008; Nielsen & Clemmensen 2009; Clemmensen *et al*. 2012; Hede *et al*. 2015).

In this study, we use optically stimulated luminescence (OSL) to date raised beach ridges from Gjellerodde near Lemvig in the western part of Limfjorden. Our aim is to: (1) constrain the Late Holocene RSL changes, and (2) link the formation of beach ridges to periods when there was an open connection between the Limfjord and the North Sea.

2. Study site

Gjellerodde is a cuspate foreland in Jylland, west Denmark (Fig. 1). It is located at the entrance of Lemvig, a tributary fjord of the 150 km long Limfjord estuary that separates Vendsyssel (to the north) from the rest of Jylland. Gjellerodde lies east of a 40 m high moraine plateau (Gjellerbakker) and is a relatively flat low-lying area, primarily covered by heath and small patches of localised forest. A fossil coastline representing the Littorina sea cliff is cut into the moraine plateau (Jessen 1910; Mertz 1924; Jessen 1936). Gjellerodde consists of postglacial marine sediments composed of numerous gravelly beach ridges. The northern coast is affected by human activity, as the Danish Coastal Authority engages in beach nourishment to protect against erosion. Gjellerodde is bisected by an
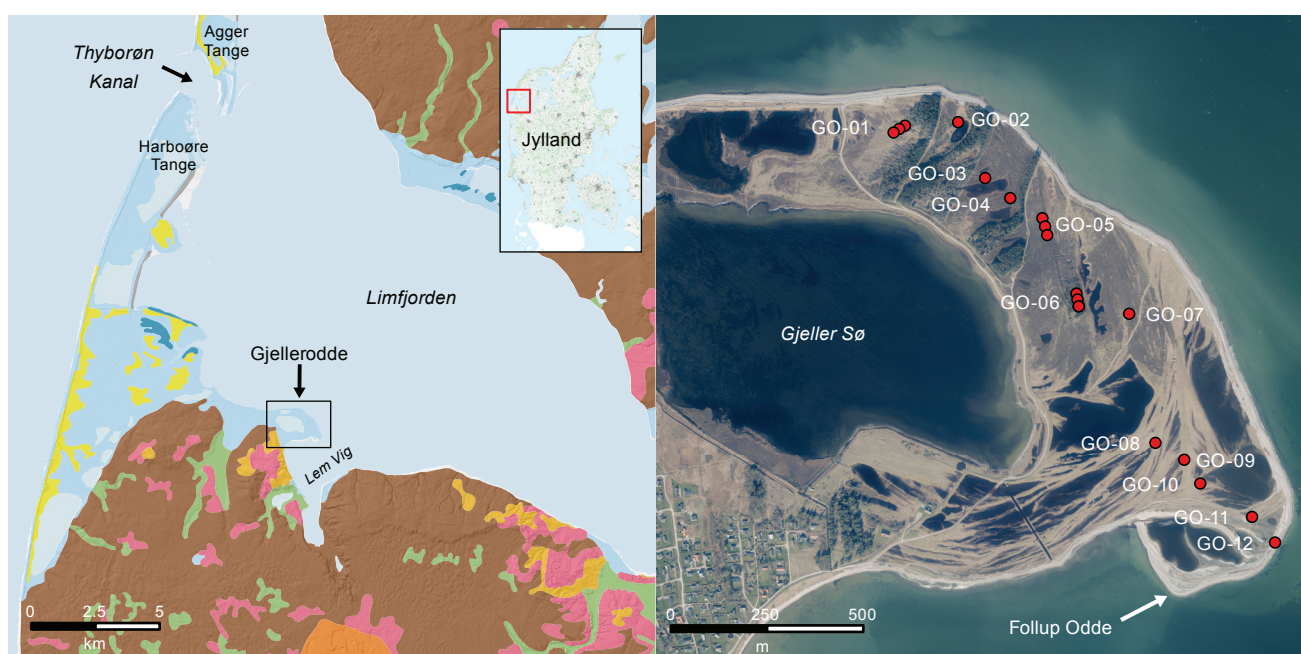
Fig. 1 Overview of the study area. **Left**: map of Gjellerodde in relation to the opening to the North Sea at Thyborøn Kanal. **Right:** aerial photograph of Gjellerodde overlain with the digital elevation model (DEM) hillshade map. Sampling site locations are marked in **red**, alongside the sample name. The coastal barrier through which the Thyborøn Kanal flows, consists of Harboøre Tange and Agger Tange; collectively known as Limfjordstangerne.

artificial levee, built between 1869 and 1871 (Skovborg 1957). Trenches were dug into and in between some of the beach ridges during World War II. The trenches are located between sites GO-05 and GO-06 and were avoided during sampling. Today the area is protected as a bird habitat under the Natura 2000 program, administered by Lemvig Municipality and is used as a grazing area for sheep. The south-eastern section of Gjellerodde, known as Follup Odde, is presently expanding. Follup Odde is first visible on maps from 1839 (Branner 1839) and likely only started forming in the beginning of the 1800s (Jessen 1936).

From the morphology of Gjellerodde and the beach ridges it seems that the present-day sediment transport is controlled by two coastal currents. One current flows west to east from Thyborøn Canal through Limfjorden. The other current within Lem Vig flows north to south. These two currents form a right angle of sediment transport.

The sample sites were chosen to give the best possible indication of the chronological formation of Gjellerodde, by choosing sites located on the different ridges. A total of 19 sediment samples were collected from Gjellerodde. Figure 1 shows an aerial photograph overlain with the digital elevation model (DEM) hillshade map to enhance ridge visibility. In Fig. 1 the sampling sites are marked in red with the site name. Coordinates and sampling depth were noted for each sample location. At sites GO-1, GO-5 and GO-6, multiple samples were taken to test reproducibility. Samples were taken by digging approximately 60–70 cm vertically into the ridge. To enable infinite dose matrix interpretation of measured dose rates the sample is taken >30 cm from non-homogeneous sediment layers. Samples were taken by inserting a metal pipe (length: 20–25 cm, diameter: 5 cm) horizontally into the ridge. The ends were sealed to prevent light contamination to the sample. The sediment samples from GO-01 to GO-07 consist of coarse-grained sand and gravel whereas samples GO-08 to GO-12 consist mainly of coarse-grained sand.

3. Methods

3.1 Sample preparation
The samples were prepared according to standard procedures under subdued red-orange light (Aitken 1985). The outer approximately 5 cm of each sample tube was removed and used to estimate the concentration of radionuclides and water content (w.c.). In order to isolate quartz and potassium-rich feldspar from the sediment within each sample tube, a series of steps were carried out (Aitken 1985) as follows: (1) The sediment from the inner part of each sample tube was sieved using a mesh size of 180–250 μm. (2) The sieved

sediment was subjected to a cleaning process using hydrochloric acid and hydrogen peroxide. (3) To remove the outer 10 μm layer of grains affected by alpha irradiation, a chemical treatment involving 10% hydrofluoric (HF) acid was employed. (4) Heavy liquid separation was performed (density of 2.58 g/cm³) to separate quartz and potassium feldspar. (5) Finally, the extracted quartz was further treated with a 40% HF acid solution.

3.2 Measurement facilities
The luminescence measurements were conducted with Risø thermoluminescence (TL)/OSL readers equipped with blue (λ = 470 nm, approximately 80 mW/cm²) and IR (λ = 870 ± 40 nm, approximately 130 mW/cm²) stimulation light sources, as described by Bøtter-Jensen et al. (2010). For detecting the emitted luminescence EMI 9635QA photomultipliers were employed accompanied by 7.5 mm thick Hoya U-340 glass filters. The beta irradiation was performed using calibrated 90Sr/90Y sources mounted on the readers, following the procedures outlined by Bøtter-Jensen et al. (2010) and Hansen et al. (2015).

To measure the bulk-radionuclide concentrations, high-resolution gamma spectrometry was employed, as described by Murray et al. (1987) and Murray et al. (2018). In order to prevent radon loss and ensure a consistent counting setup, sediment samples were heated to 50°C and embedded in wax, following the methodology outlined by Murray et al. (1987). To allow sufficient time for equilibrium between ^{222}Rn and its parent ^{226}Ra before measurement, the cast samples were stored for a minimum of 3 weeks, as recommended by Murray et al. (1987). The conversion of bulk-radionuclide concentrations into infinite matrix dose rates was accomplished by applying the conversion factors and grain size attenuation factors established by Guérin et al. (2011) and Guérin et al. (2012), respectively. For the internal quartz alpha dose rate, a value of 0.020 ± 0.010 Gy/ka was assumed based on Vandenberghe et al. (2008). Cosmic ray dose rates were calculated according to Prescott and Hutton (1994), considering the current burial depths and assuming a 5% uncertainty. The long-term w.c. was set at 18% of the saturated w.c., which was determined as the average value for all samples. An uncertainty of 4% was assumed for the w.c.

Changing the long-term w.c. value from 0 to 100% of saturated w.c. does not reveal any minimum relative standard error (RSE). Consequently, when analysing errors, it is not possible to draw any conclusions regarding which assumption is the best. Using the current w.c. also does not change the RSE.

3.3 Optically stimulated luminescence
The OSL dating method is useful for establishing the absolute chronology of most sediments, revealing when they were last exposed to daylight. OSL exploits the behaviour

of electrons within the crystal structures of quartz and feldspar. When sediment is buried, shielding it from sunlight, mineral grains (quartz and feldspar) within the sediment accumulate a latent luminescence signal. This accumulation occurs due to the interaction with ionising radiation emitted primarily by naturally occurring U- and Th-series, K-40, and cosmic rays. By subjecting the grains to optical stimulation, the intensity of the OSL signal can be measured and calibrated in terms of absorbed dose, known as the equivalent dose ($\dot{D}_e$) in Gy. To determine the burial age, the $\dot{D}_e$ is divided by the environmental dose rate ($\dot{D}$), expressed in Gy/ka. The environmental dose rate is determined through independent measurements such as high-resolution gamma spectrometry. The calculation of equivalent doses in this study employed the single-aliquot regenerative dose (SAR) procedure, as established by Murray and Wintle (2000; see Section 3.3.1). During the formation of the beach ridge, sediment deposition is assumed to have resulted in exposure to sunlight. This exposure, known as bleaching, acts as a resetting mechanism, providing a measurable age of the sediment.

3.3.1 Multi-grain quartz OSL measurements

Dose measurements were conducted on multi-grain quartz aliquots using the SAR procedure, as described by Murray & Wintle (2000). Blue light stimulation was applied for 40 s at 125°C to acquire the measurements, with the intention of avoiding significant accumulation of photo-transferred thermoluminescence (PTTL) in the 110°C peak. To minimise potential recuperation effects, a 280°C blue stimulation for 40 s was included between each SAR cycle, following the approach outlined by Murray & Wintle (2003). The aliquots were prepared on stainless steel cups using an 8 mm spot of silicon oil, resulting in approximately 2000 grains per aliquot, as described by Duller (2008). To optimise the contribution of the fast-component in the OSL signal used for calculations, an early background subtraction technique was employed based on the method proposed by Ballarini et al. (2007).

The main objective of the SAR protocol is to determine the radiation dose equivalent to the natural luminescence signal measured from the sample. The estimation of equivalent dose relies on a minimum of three sensitivity-corrected regeneration points, along with a recuperation point and a recycling point. Individual dose-response curves (DRCs) were fitted using a single saturation exponential function that passes through the origin, as described in Murray et al. (2021). To derive equivalent doses, interpolation of the sensitivity-corrected natural signal on the individual DRCs was performed. Average equivalent dose values were calculated using an unweighted arithmetic mean, following the methodology outlined by Guérin et al. (2017). The provided uncertainty represents the standard error at a 68% confidence level. To identify and eliminate individual dose values that deviated significantly, the inter-quartile rejection (IQR) criterion, proposed by Medialdea et al. (2014), was applied. Dose values exceeding 1.5 interquartile ranges above the upper quartile (75%) or below the lower quartile (25%) were rejected. To determine the most suitable SAR protocol for this study, a preheat plateau test and a dose-recovery preheat plateau test were conducted. Different preheat temperatures ranging from 160 to 260°C, with a cut heat of 40°C, were tested. A stable plateau up to a preheat 220°C was observed in the preheat plateau test. The estimated dose-to-given-dose ratio was evaluated with a given dose of c. 6 Gy. The selected protocol in this study involved a preheat temperature of 200°C, with a recovery ratio and an infrared (IR) depletion ratio consistent with unity (1.00 ± 0.04, n = 6) and (0.99 ± 0.04, n = 6), respectively. No significant thermal transfer was observed (0.021 ± 0.017 Gy, n = 6). Additionally, an insignificant recuperation of 0.1 ± 0.3% (n = 6) was observed.

3.3.2 Multi-grain feldspar infrared stimulated luminescence (IRSL) measurements

In all K-rich feldspar dose measurements, a preheat temperature of 250°C was applied for a duration of 100 s. The multi-grain K-rich feldspar aliquots were stimulated using IR light at 50°C for 200 s, followed by an additional IR stimulation at 225°C for 200 s. This particular stimulation protocol, known as IR_{50} and post-IR IRSL 225 ($PIRIR_{225}$), was adopted based on the methodology introduced by Buylaert et al. (2012). To minimise potential recuperation effects, a test dose approximately equal to the natural dose magnitude was employed, and a high-temperature IR bleach was performed at 265°C for 200 s between successive SAR cycles. For dose estimation, the light emitted during the initial 2 s of stimulation was considered, while the contribution from the last 10 s of stimulation was subtracted using a late background subtraction (LBG) approach. The aliquots were prepared on stainless steel cups, using a 2 mm spot of silicon oil, resulting in an approximate count of 100 grains per aliquot, following the methodology described by Duller (2008).

4. Results

The radionuclide concentrations derived by using high-resolution gamma spectrometry are summarised in Table 1. The dry infinite matrix beta and gamma dose rates are also given, derived assuming a 20 ± 10% loss of ^{222}Rn compared to its parent ^{226}Ra. Total dose rates, also given in Table 1, include the contribution from cosmic rays, internal dose rates, and the effects of w.c. 18% of saturated w.c.

Table 1 Dose rate summary.

Sample no.	Site no.	Depth (cm)[a]	w.c. (%)	Radionuclide concentrations (Bq/kg)				Infinite matrix dry dose rates (Gy/ka)		Total dose rates (Gy/ka)	
				^{238}U	^{226}Ra	^{232}Th	^{40}K	Beta	Gamma	KF[b]	Q[b]
224501	GO-01	41	6	15 ± 2	8.2 ± 0.4	5.9 ± 0.3	220 ± 6	0.68 ± 0.02	0.300 ± 0.007	2.01 ± 0.08	1.08 ± 0.05
224502	GO-01	45	5	8 ± 2	6.6 ± 0.2	8.8 ± 0.2	242 ± 5	0.735 ± 0.013	0.340 ± 0.005	2.11 ± 0.08	1.17 ± 0.06
224503	GO-01	50	5	7 ± 2	6.2 ± 0.3	6.7 ± 0.2	273 ± 5	0.796 ± 0.013	0.337 ± 0.007	2.15 ± 0.09	1.21 ± 0.06
224504	GO-02	45	6	9 ± 3	4.7 ± 0.3	4.8 ± 0.3	355 ± 7	0.97 ± 0.02	0.369 ± 0.008	2.31 ± 0.09	1.38 ± 0.07
224505	GO-03	30	6	3 ± 2	5.1 ± 0.4	4.6 ± 0.2	251 ± 6	0.72 ± 0.02	0.288 ± 0.007	2.05 ± 0.08	1.11 ± 0.05
224506	GO-04	34	5	6 ± 2	4.9 ± 0.2	4.8 ± 0.2	278 ± 5	0.783 ± 0.014	0.310 ± 0.006	2.12 ± 0.08	1.19 ± 0.06
224507	GO-05	37	5	3 ± 2	5.4 ± 0.3	7.7 ± 0.2	247 ± 5	0.729 ± 0.013	0.323 ± 0.007	2.09 ± 0.08	1.15 ± 0.06
224508	GO-05	38	6	7 ± 2	8.6 ± 0.2	9.5 ± 0.2	217 ± 4	0.697 ± 0.012	0.343 ± 0.008	2.08 ± 0.08	1.14 ± 0.05
224509	GO-05	22	6	5 ± 2	4.7 ± 0.3	5.1 ± 0.2	205 ± 5	0.599 ± 0.013	0.254 ± 0.006	1.93 ± 0.08	1.00 ± 0.05
224510	GO-06	44	5	7 ± 2	6.3 ± 0.3	7.7 ± 0.2	297 ± 6	0.865 ± 0.015	0.369 ± 0.008	2.25 ± 0.09	1.31 ± 0.06
224511	GO-06	52	5	6 ± 2	6.2 ± 0.3	7.6 ± 0.2	304 ± 5	0.881 ± 0.014	0.372 ± 0.007	2.26 ± 0.09	1.32 ± 0.07
224512	GO-06	45	5	8 ± 2	6.3 ± 0.3	8.2 ± 0.3	307 ± 6	0.89 ± 0.02	0.383 ± 0.008	2.28 ± 0.09	1.35 ± 0.07
224513	GO-06	75	5	7 ± 2	4.4 ± 0.3	5.5 ± 0.2	258 ± 6	0.73 ± 0.02	0.299 ± 0.007	2.04 ± 0.08	1.11 ± 0.05
224514	GO-07	48	5	7 ± 2	5.7 ± 0.3	7.1 ± 0.2	172 ± 5	0.538 ± 0.013	0.259 ± 0.007	1.86 ± 0.08	0.92 ± 0.04
224515	GO-08	42	5	5 ± 2	5.1 ± 0.4	5.3 ± 0.2	152 ± 5	0.471 ± 0.014	0.218 ± 0.007	1.77 ± 0.07	0.84 ± 0.04
224516	GO-09	40	5	7 ± 2	6.1 ± 0.3	7.3 ± 0.2	216 ± 5	0.654 ± 0.014	0.299 ± 0.007	2.00 ± 0.08	1.06 ± 0.05
224517	GO-10	40	5	6 ± 2	6.1 ± 0.3	6.9 ± 0.2	224 ± 5	0.674 ± 0.014	0.301 ± 0.007	2.02 ± 0.08	1.08 ± 0.05
224518	GO-11	32	6	8 ± 2	7.1 ± 0.3	7.4 ± 0.3	197 ± 5	0.617 ± 0.014	0.291 ± 0.008	1.97 ± 0.08	1.03 ± 0.05
224519	GO-12	30	6	5 ± 3	3.7 ± 0.6	3.9 ± 0.4	124 ± 7	0.38 ± 0.02	0.169 ± 0.009	1.66 ± 0.07	0.72 ± 0.03

Dry infinite matrix dose rates are derived from radionuclide concentrations measured using high-resolution gamma spectrometry. Total dose rates include the contribution from cosmic rays, internal dose rates and the effects of water content (w.c.). [a]Depths below current surface are given in cm. [b]Q and KF refer to dose rates of quartz and K-rich (12.60 ± 0.15%) feldspar, respectively.

Table 2 Summary of multi-grain quartz results (OSL) and multigrain potassium-rich feldspar results (IR$_{50}$ and pIRIR$_{225}$).

Sample no.	Site no.	Elevation (m a.s.l.)	Dose (Gy)[a]									Age (ka)[b]		
			IR$_{50}$	n_r	n_a	pIRIR$_{225}$	n_r	n_a	OSL	n_r	n_a	IR$_{50}$	pIRIR$_{225}$	OSL
224501	GO-01	1.56	5.5 ± 0.2	1	11	10.5 ± 0.5	1	11	3.51 ± 0.10	2	16	3.7 ± 0.3	5.0 ± 0.3	3.26 ± 0.19
224502	GO-01	1.80	5.23 ± 0.09	2	10	9.7 ± 0.5	1	10	3.79 ± 0.11	1	14	3.5 ± 0.2	4.6 ± 0.3	3.2 ± 0.2
224503	GO-01	1.99	6.04 ± 0.19	0	18	10.2 ± 0.4	2	16	4.5 ± 0.3	2	21	3.9 ± 0.2	4.8 ± 0.3	3.7 ± 0.3
224504	GO-02	1.62	6.22 ± 0.11	0	12	11.32 ± 0.18	1	11	4.14 ± 0.09	0	18	3.61 ± 0.19	4.9 ± 0.2	3.01 ± 0.17
224505	GO-03	1.42	5.38 ± 0.21	0	12	9.1 ± 0.4	0	12	3.86 ± 0.17	1	17	3.32 ± 0.15	4.4 ± 0.3	3.5 ± 0.2
224506	GO-04	2.08	5.22 ± 0.09	1	11	9.6 ± 0.3	0	12	3.50 ± 0.11	0	18	3.36 ± 0.18	4.5 ± 0.3	2.95 ± 0.18
224507	GO-05	2.92	4.96 ± 0.12	0	12	8.0 ± 0.2	1	11	3.18 ± 0.07	2	16	3.17 ± 0.17	3.8 ± 0.2	2.76 ± 0.15
224508	GO-05	3.10	4.66 ± 0.07	3	9	8.3 ± 0.2	0	12	3.01 ± 0.08	0	18	3.05 ± 0.18	4.0 ± 0.2	2.64 ± 0.15
224509	GO-05	2.89	4.57 ± 0.15	0	12	7.7 ± 0.5	0	12	2.74 ± 0.07	2	16	3.15 ± 0.16	4.0 ± 0.3	2.75 ± 0.15
224510	GO-06	2.68	6.50 ± 0.19	2	10	14.2 ± 1.1	0	12	3.62 ± 0.09	1	17	3.9 ± 0.2	6.3 ± 0.6	2.77 ± 0.16
224511	GO-06	2.62	6.13 ± 0.19	0	12	11.3 ± 0.5	0	12	3.70 ± 0.12	1	17	3.64 ± 0.18	5.0 ± 0.3	2.81 ± 0.18
224512	GO-06	2.59	7.3 ± 0.3	0	12	12.9 ± 0.8	1	11	3.69 ± 0.08	1	17	4.1 ± 0.3	5.7 ± 0.4	2.74 ± 0.16
224513	GO-06	2.59	6.1 ± 0.2	1	11	11.4 ± 0.5	0	12	3.34 ± 0.09	0	18	3.9 ± 0.2	5.6 ± 0.3	3.02 ± 0.18
224514	GO-07	2.81	4.67 ± 0.14	0	12	7.6 ± 0.2	2	10	2.55 ± 0.10	0	18	3.42 ± 0.18	4.1 ± 0.2	2.75 ± 0.18
224515	GO-08	1.49	2.99 ± 0.17	1	9	6.6 ± 0.7	0	10	2.5 ± 0.4	3	15	2.21 ± 0.15	3.7 ± 0.4	3.0 ± 0.5
224516	GO-09	1.44	2.99 ± 0.14	2	8	9 ± 2	1	9	1.34 ± 0.07	1	21	2.04 ± 0.14	4.3 ± 1.0	1.26 ± 0.09
224517	GO-10	1.10	2.7 ± 0.2	0	5	5.8 ± 0.8	1	4	1.22 ± 0.13	4	18	1.8 ± 0.2	2.9 ± 0.4	1.13 ± 0.14
224518	GO-11	1.05	6.5 ± 1.6	1	4	22 ± 3	0	5	0.27 ± 0.05	2	11	4.5 ± 1.2	11 ± 2	0.27 ± 0.05
224519	GO-12	0.96	0.87 ± 0.12	0	8	4.3 ± 0.5	0	8	0.10 ± 0.03	3	24	0.70 ± 0.10	2.6 ± 0.3	0.14 ± 0.04

a.s.l.: above sea level. [a]Dose is the arithmetic average equivalent dose after the application of the IQR criterion. All uncertainties are reported at the 68% confidence interval. [b]Age ′ is the equivalent dose divided by the total dose rate (see Table 1). n_a: number of aliquots included in the equivalent dose estimation, that is the total number of measured aliquots less the number of dose estimates rejected by the IQR criterion. n_r: number of dose estimates rejected by the IQR criterion. The IR$_{50}$ ages were fading-corrected using a g-value of 2.82 ± 0.19%/decade. The pIRIR$_{225}$ ages were not corrected for fading.

Equivalent doses and ages are given in Table 2. The IR$_{50}$ ages were fading corrected using a g-value of 2.82 ± 0.19%/decade (n = 6). Figure 2 shows feldspar IRSL ages (feldspar) plotted versus OSL ages (quartz). The bleaching rate of feldspar is lower than that of quartz. Thus the relation between feldspar IRSL ages and quartz OSL ages can account for the extent of bleaching of the quartz grains at the time of deposition. The feldspar components of the sediment sample should preferably not be older than the quartz.
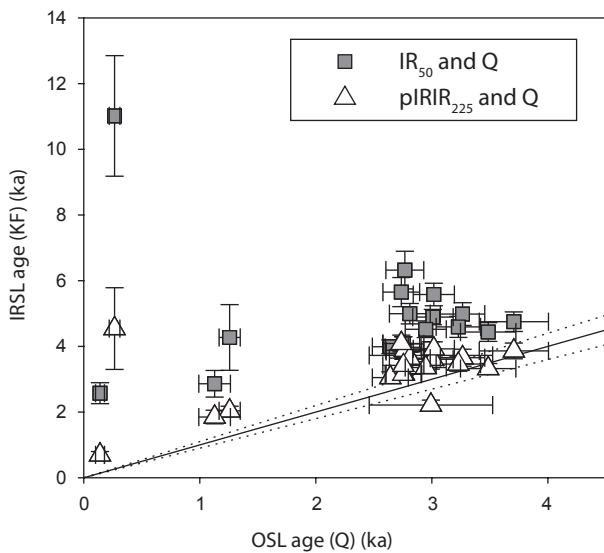
Fig. 2 IR$_{50}$ ages (grey squares) and pIRIR$_{225}$ ages (white triangles) from K-rich feldspars (KF) versus OSL ages from quartz (Q). The IR$_{50}$ ages were fading-corrected using a g-value of 2.82 ± 0.19%/decade. A 1:1 line is shown **(black line)** with ± 10% **(dotted lines)**.

Figure 2 shows a good correlation between OSL quartz and pIRIR$_{225}$ ages and we conclude that the quartz grains were indeed well-bleached at deposition. Note the IR$_{50}$ signals give older ages than the OSL quartz and pIRIR$_{225}$ signals. This overestimation may result from the correction for fading of the IR signals in these young samples. Nevertheless, the OSL quartz ages presented here are considered reliable given their agreement with those obtained by pIRIR$_{225}$.

4.1 Beach-ridge chronology

Figure 3 shows OSL ages (i.e. burial age) at the sample position. As expected, given the spatial locations of the beach ridges from inner to outer locations and beach progradation from oldest to youngest, there is a general decrease in age from north-west to south-east, with few exceptions. Figure 4 shows the OSL ages alongside sample elevation. The OSL ages of all samples decrease
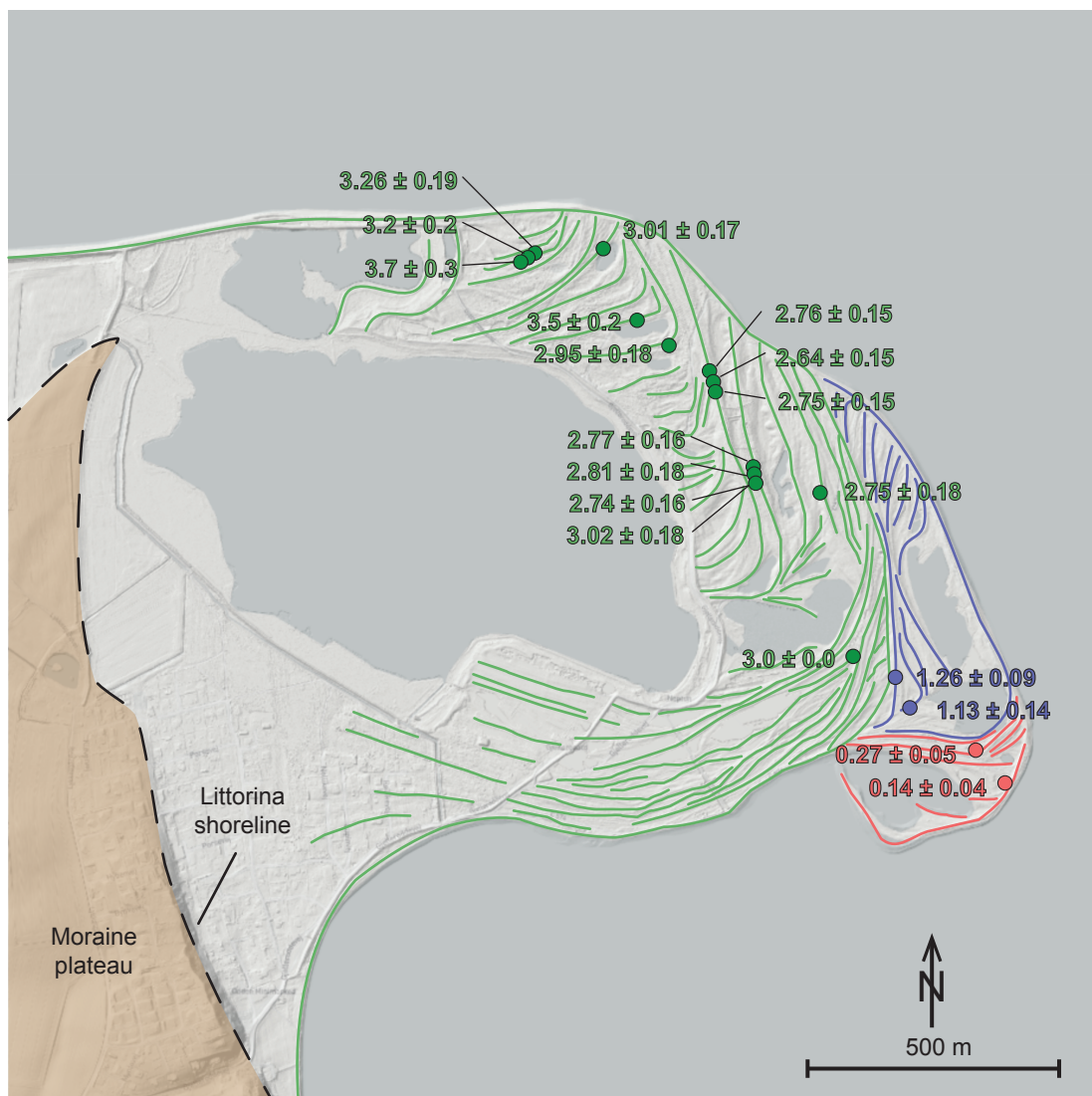

Fig. 3 OSL ages (ka) and one standard error (including systematic errors). Samples are colour coded green, blue and red according to the three phases of beach-ridge formation identified at Gjellerodde (see Fig. 4 for details of these three events).
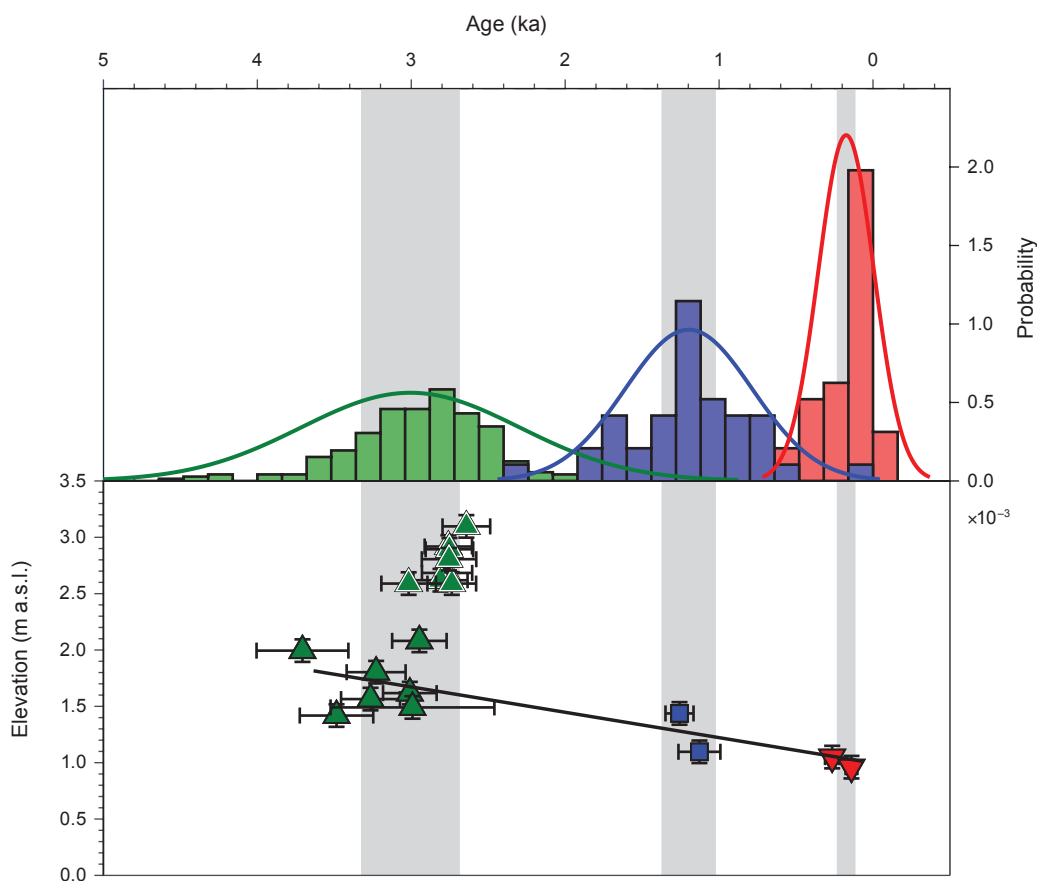
Fig. 4 Three distinct groups of OSL ages identified for beach-ridge formation in Gjellerodde. **Top**: histograms and probability distribution functions for the three groups identified in the lower panel, shown in green, blue and red. **Lower**: OSL ages (ka) shown with one standard error (including systematic errors) and their elevation (m). Grey shading indicates the three distinct groups of ages defined by the range of data in that group including random and systematic errors at the 95% significant level. Groups were identified by a one-way ANOVA test on all samples at the 95% significant level. Dark green triangles with black outline: samples <2.5 m elevation. Green triangles with white outline: samples >2.5 m elevation. See also Fig. 3. The solid black line represents a linear interpolation excluding the highest beach ridges.

from high to low sample elevations, again with few exceptions.

All OSL ages were analysed using one-way ANOVA test, which identified three groups of ages at the 95% significant level. The samples within each group are positioned in a way that corresponds to their geographical location, with the oldest group of samples situated at the highest elevation and the youngest at the lowest elevation (Fig. 4). The oldest group is located farthest north-west and the youngest towards the south-east (see Fig. 3). Based on elevation the oldest group can be divided into two, in which the most elevated beach ridges (white-edged triangles in Fig. 4) yield younger ages than some of morphostratigraphically older ridges located at lower elevations (black-edged triangles in Fig. 4). Evaluating deposition rate by including only the lowest beach ridges of the oldest group of samples gives deposition rates of *c.* 0.2 mm/year (solid black line in Fig. 4).

5. Discussion

5.1 RSL changes in the Late Holocene

The OSL ages (now corrected to years before present (BP), i.e. before 1950) for the raised beach ridges are plotted together with the existing RSL data from Limfjorden as recently reviewed by Bennike *et al.* (2019) and Jessen *et al.* (2019; Fig. 5a). Overall, the OSL ages fall on the projected sea-level curve which represents a straight line from a maximum RSL *c.* 3 m above sea level (a.s.l.; Mertz 1924) approximately 7000 years BP to the present-day sea level. However, some of the OSL ages from the highest-elevated beach ridges are younger than some of the morphostratigraphically older ridges located at lower elevations (Figs 4 and 5b). This indicates that the RSL remained high at *c.* 3 m a.s.l. until 3 ka followed by a fairly rapid fall – something that has not been recorded in other records from the area (Bennike *et al.* 2019; Kristiansen *et al.* 2021). Instead, we suggest that these beach
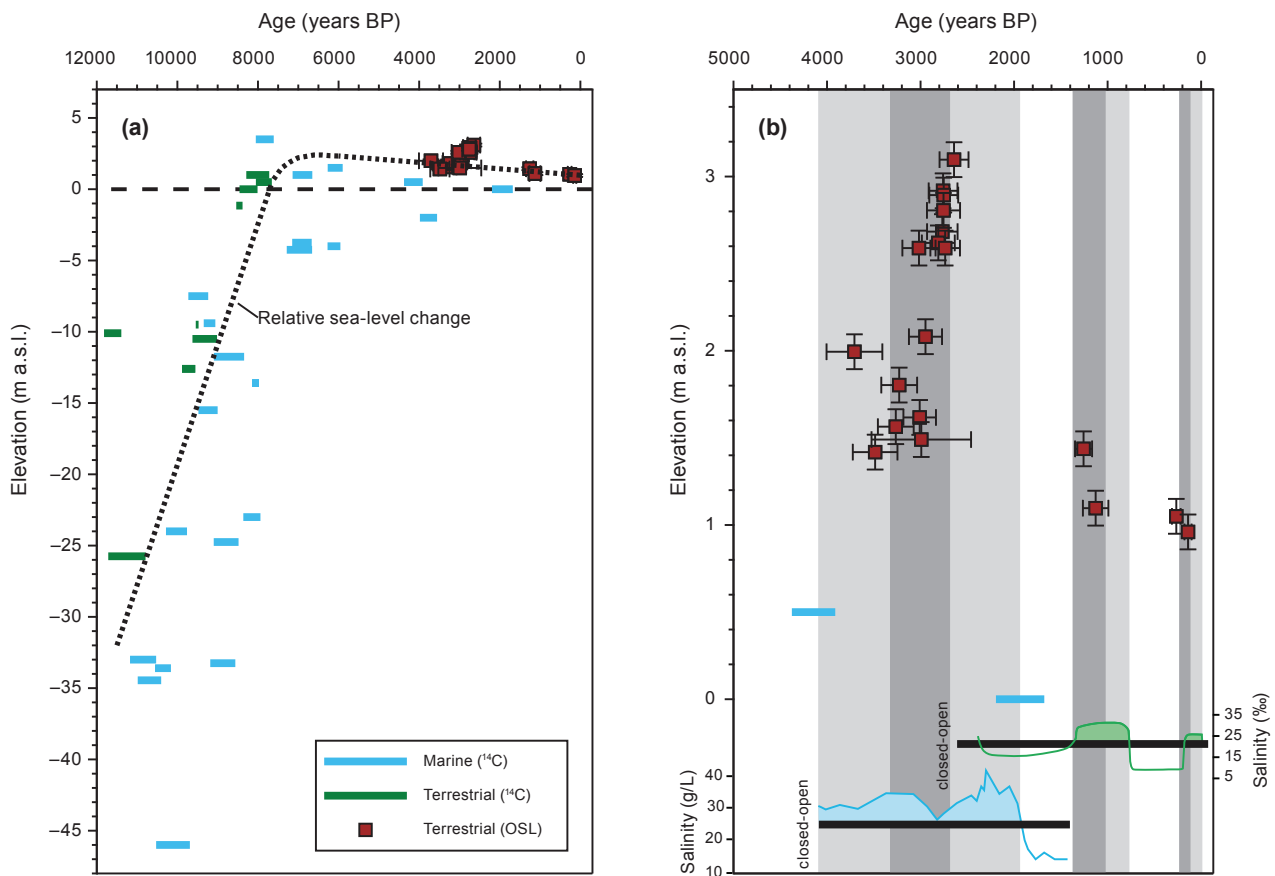
Fig. 5 Comparison of OSL ages from this study with previously published radiocarbon histories and palaeo-salinity data. **a:** Holocene RSL curve (**dashed curve**) for Limfjorden based on radiocarbon-dated samples (Bennike *et al*. 2019; Jessen *et al*. 2019) and OSL ages (this study) vs. elevation (m). All ages are in years BP (i.e. before 1950). Error bars are one standard error. Marine and terrestrial 14C ages are shown in blue and green, respectively. **b:** The same OSL ages are shown alongside palaeo-salinity data for the Limfjord (Kristensen *et al*. 1995; Lewis *et al*. 2013). High salinity indicates an open connection towards the North Sea (Kristensen *et al*. 1995; Lewis *et al*. 2013). Dark grey shading indicates periods when the connection between the Limfjord and the North Sea was open according to the OSL ages (this study) and the light grey shading indicates open periods according to salinity concentrations (Kristensen *et al*. 1995; Lewis *et al*. 2013).

ridges are unrelated to a specific sea level and formed under an extraordinary storm event that produced some extraordinarily high beach ridges (Clemmensen *et al*. 2012). Accordingly, we place the RSL curve through the oldest group of OSL ages *c.* 1.5–2 m a.s.l. (Figs 4 and 5a). Using a simple linear interpolation that excludes the highest beach ridges suggests a drop in RSL of *c.* 1 m in the last 3000 years, that is *c.* 0.2 mm/yr (Fig. 4). This estimate is lower than estimates from Nørholm in the northern part of the Limfjord where the rate of sea-level change was estimated to be *c.* 1.2±0.2 mm/yr in the last 3000 years (Kristiansen *et al*. 2021). The difference between the two sites is, however, expected as Gjelleroddde is located *c.* 75 km south-west where the average long-term isostatic rates of uplift are lower (*c.* 0.25 mm/yr) and in line with our estimates (Hansen *et al*. 2012). Although our results overall are consistent with previous investigations, we acknowledge that beach-ridge formation is not only controlled by changes in RSL and that sediment supply and wind regime may also play an important role.

5.2 Beach-ridge formation as a potential indicator for an open Limfjord – North Sea connection

The new OSL ages presented here indicate that beach ridges did not develop continuously in the Late Holocene but were formed during three discrete periods 3.3–2.7, 1.4–1.0, 0.2–0.1 ka (Fig. 4). However, because only a subset of the beach ridges were dated we cannot rule out the possibility that they also formed in other time periods or that the existing periods should be expanded. The formation of the most recent beach ridges is related to the recent opening in 1825 CE (Gram-Jensen 1991) and this formation of new beach ridges has continued until the present-day. The second and third succession of beach ridges comprise most of the beach ridges at Gjelleroddde and they were formed 3.3–2.7 and 1.4–1.0 ka. Both periods coincide with increased salinity in the Limfjord indicating full marine conditions and open connections to the North Sea (Kristensen *et al*. 1995; Lewis *et al*. 2013). It is interesting to see that some of the beach ridges date to the Viking Age (793–1066 CE, see the central group (blue)

in Fig. 4) when it has been speculated that an opening to the west existed (Eriksen *et al*. 2009). According to these accounts, the opening to the west closed shortly after the Viking Age (Eriksen *et al*. 2009) in agreement with the OSL-beach-ridge chronology (1.4–1.0 ka).

Overall, our data indicate that OSL dating of beach ridges may indicate an open Limford – North Sea connection. The open connection would have facilitated a stronger current that would increase erosion and this would have been the dominant factor in producing the beach ridges at Gjellerodde and possibly in a more extensive area in the western Limfjord area. Other factors may also have influenced the formation of beach ridges including changes in storm intensity, currents, and sediment availability. However, to test this hypothesis would require investigation of more beach ridge systems to link their timing of formation with geomorphological processes in the western Limfjord.

6. Conclusions

In this study, we used OSL dating of beach ridges in combination with existing sea-level proxy data to determine Late Holocene sea-level changes and identify when the Limfjord was last connected to the North Sea. Based on 19 OSL ages from beach ridges at Gjellerodde, the Late Holocene rate of RSL change was estimated to be *c.* 0.2 mm/yr, consistent with other estimates from northern Denmark. Our OSL ages furthermore indicate that the beach ridges at Gjellerodde were most likely formed during three discrete time periods at 3.3–2.7, 1.4–1.0, 0.2–0.1 ka. Overall there is a good correlation between known historical accounts and paleoenvironmental reconstructions of salinity changes and the formation of beach ridges in the western Limfjord. Accordingly, this suggests that OSL dating of beach ridges can be used as an indicator for determining when there was an open connection between the western Limfjord and the North Sea in the Late Holocene.

Acknowledgements

Additional information

Author contributions

THF, CFR & NKL: conceptualisation of the study and supervision. LRB, MB, EH: fieldwork, OSL measurements and data analysis. THF, LRB, MB, EH, CFR & NKL: data interpretation and writing the first draft of the manuscript.

Competing interests

The authors declare that there are no competing interests.

References

Aitken, M.J. 1985: Thermoluminescence dating. London: Academic Press.

Ballarini, M., Wallinga, J., Wintle, A.G. & Bos, A.J.J. 2007: A modified SAR protocol for optical dating of individual grains from young quartz samples. Radiation Measurements **42**, 360–369. *https://doi.org/10.1016/j.radmeas.2006.12.016*

Bennike, O., Nørgaard-Pedersen, N., Jensen, J., Andresen, K. & Seidenkrantz, M.-S. 2019: Development of the western Limfjord, Denmark, after the last deglaciation: a review with new data. Bulletin of the Geological Society of Denmark **67**, 53–73. *https://doi.org/10.37570/bgsd-2019-67-04*

Bøtter-Jensen, L., Thomsen, K.J. & Jain, M. 2010: Review of optically stimulated luminescence (OSL) instrumental developments for retrospective dosimetry. Radiation Measurements **45**, 253–257. *https://doi.org/10.1016/j.radmeas.2009.11.030*

Branner, W. 1839: Sognekort, Tørring Sogn (Skodborg Herred) 1839. Historiske kort pa nettet. Nørresundby: Geodatastyrelsen.

Buylaert, J.-P., Jain, M., Murray, A.S., Thomsen, K.J., Thiel, C. & Sohbati, R. 2012: A robust feldspar luminescence dating method for middle and late pleistocene sediments. Boreas **419**, 435–451. *https://doi.org/10.1111/j.1502-3885.2012.00248.x*

Clemmensen, L., Murray, A. & Nielsen, L. 2012: Quantitative constraints on the sea-level fall that terminated the Littorina Sea Stage, southern Scandinavia. Quaternary Science Reviews **40**, 54–63. *https://doi.org/10.1016/j.quascirev.2012.03.001*

Duller, G.A.T. 2008: Single-grain optical dating of quaternary sediments: why aliquot size matters in luminescence dating. Boreas **37**, 589–612. *https://doi.org/10.1111/j.1502-3885.2008.00051.x*

Eriksen, P., Egeberg, T., Olesen, L. & Rostholm, H. 2009: Vikinger i vest. Vikingetiden i Jylland. 70. Aarhus: Jysk Arkæologisk Selskabs Skrifter.

Goodwin, I.D., Stables, M.A. & Olley, J.M. 2006: Wave climate, sand budget and shoreline alignment evolution of the iluka-woody bay sand barrier, northern New South Wales, Australia, since 3000 yr bp. Marine Geology **226**(1), 127–144. *https://doi.org/10.1016/j.margeo.2005.09.013*

Gram-Jensen, I. 1991: Stormfloder. Danish Meteorological Report, 91-1, 121 p.

Guérin, G., Mercier, N. & Adamiec, G. 2011: Dose-rate conversion factors: update. Ancient TL **29**, 5–8.

Guérin, G., Mercier, N., Nathan, R., Adamiec, G. & Lefrais, Y. 2012: On the use of the infinite matrix assumption and associated concepts: a critical review. Radiation Measurements **47**(9), 778–785. *https://doi.org/10.1016/j.radmeas.2012.04.004*

Guérin, G. *et al*. 2017: Absorbed dose, equivalent dose, measured dose rates, and implications for OSL age estimates: introducing the average dose model. Quaternary Geochronology **41**, 163–173. *https://doi.org/10.1016/j.quageo.2017.04.002*

Hansen, J., Aagaard, T. & Binderup, M. 2012: Absolute sea levels and isostatic changes of the eastern north sea to central Baltic region during the last 900 years. Boreas **41**, 180–208. *https://doi.org/10.1111/j.1502-3885.2011.00229.x*

Hansen, V., Murray, A.S., Buylaert, J.-P., Yeo, E.Y. & Thomsen, K.J. 2015: A new irradiated quartz for beta source calibration. Radiation Measurements **81**, 123–127. *https://doi.org/10.1016/j.radmeas.2015.02.017*

Hede, M.U., Sander, L., Clemmensen, L.B., Kroon, A., Pejrup, M. & Nielsen, L. 2015: Changes in holocene relative sea-level and coastal morphology: a study of a raised beach ridge system on Samsø, southwest Scandinavia. The Holocene **25**(9), 1402–1414. *https://doi.org/10.1177/0959683615585834*

Jessen, A. 1910: Stenalderhavets udbredelse i det nordlige jylland. Danmarks Geologiske Undersøgelse II. Række, **35**, 112 pp. *https://doi.org/10.34194/raekke2.v35.6821*

Jessen, A. 1936: Vendsyssels Geologi. Danmarks Geologiske Undersøgelse V. Række **2**, 195 p. *https://doi.org/10.34194/raekke5.v2.7010*

Jessen, C., Christensen, C. & Nielsen, B.H. 2019: Postglacial relative sea level rise in the Limfjord region, northern Jutland, Denmark. Boreas **48**(1), 119–130. *https://doi.org/10.1111/bor.12350*

Kristensen, P., Heier-Nielsen, S. & Hylleberg, J. 1995: Late-Holocene salinity fluctuations in Bjømsholm bay, Limfjorden, Denmark, as deduced from micro- and macrofossil analysis. The Holocene **5**(3), 313–322. *https://doi.org/10.1177/095968369500500306*

Kristiansen, S.M., Ljungberg, T.E., Christiansen, T.T., Dalsgaard, K., Haue, N., Greve, M.H. & Nielsen, B.H. 2021: Meadow, marsh and lagoon: Late Holocene coastal changes and human-environment interactions in northern Denmark. Boreas **50**(1), 279–293. *https://doi.org/10.1111/bor.12487*

Lewis, J.P. *et al*. 2013: Environmental change in the Limfjord, Denmark (ca 7500–1500 cal yrs bp): a multiproxy study. Quaternary Science Reviews **78**, 126–140. *https://doi.org/10.1016/j.quascirev.2013.05.020*

Medialdea, A., Thomsen, K.J., Murray, A.S. & Benito, G. 2014: Reliability of equivalent-dose determination and age-models in the OSL dating of historical and modern palaeoflood sediments. Quaternary Geochronology **22**, 11–24. *https://doi.org/10.1016/j.quageo.2014.01.004*

Mertz, E.L. 1924: Oversigt over de sen- og postglaciale niveauforandringer i danmark. Danmarks Geologiske Undersøgelse II. Række **41**, 1–49. *https://doi.org/10.34194/raekke2.v41.6827*

Murray, A.S. & Wintle, A.G. 2000: Luminescence dating of quartz using an improved single-aliquot regenerative-dose protocol. Radiation Measurements **32**, 57–73. *https://doi.org/10.1016/S1350-4487(99)00253-X*

Murray, A.S. & Wintle, A.G. 2003: The single aliquot regenerative dose protocol: potential for improvements in reliability. Radiation Measurements **37**, 377–381. *https://doi.org/10.1016/S1350-4487(03)00053-2*

Murray, A.S., Marten, R., Johnston, A. & Martin, P. 1987: Analysis for naturally occurring radionuclides at environmental concentrations by gamma spectrometry. Journal of Radioanalytical and Nuclear Chemistry **115**, 263–288. *https://doi.org/10.1007/BF02037443*

Murray, A.S., Helsted, L.M., Autzen, M., Jain, M. & Buylaert, J.-P. 2018: Measurement of natural radioactivity: calibration and performance of a high- resolution gamma spectrometry facility. Radiation Measurements **120**, 215–220. *https://doi.org/10.1016/j.radmeas.2018.04.006*

Murray, A.S., Buylaert, J.-P., Guérin, G., Qin, J., Singhvi, A.K., Smedley, R.S., & Thomsen, K.J. 2021: Optically stimulated luminescence dating using quartz sand. Nature Primer **1**, 72. *https://doi.org/10.1038/s43586-021-00068-5*

Nielsen, L. & Clemmensen, L.B. 2009: Sea-level markers identified in ground penetrating radar data collected across a modern beach ridge system in a microtidal regime. Terra Nova **21**(6), 474–479. *https://doi.org/10.1111/j.1365-3121.2009.00904.x*

Penney, D.N. 1985: The Holocene marine sequence in the løkken area of Vendsys-Sel, Denmark. EG Quaternary Science Journal **35**(1), 79–88. *https://doi.org/10.3285/eg.35.1.12*

Petersen, K.S. 1979: Den holocæne marine transgression og molluskfaunaen i hanherred – belyst ud fra en boring ved vust. Arsskrift: Dansk Geologisk Forening, 15–17.

Prescott, J.R. & Hutton, J.T. 1994: Cosmic ray contributions to dose rates for luminescence and ESR dating: large depths and long-term variations. Radiation Measurements **23**, 497–500. *https://doi.org/10.1016/1350-4487(94)90086-8*

Sander, L., Hede, M.U., Fruergaard, M., Nielsen, L., Clemmensen, L.B., Kroon, A., Johannessen, P.N., Nielsen, L.H. & Pejrup, M. 2016: Coastal lagoons and beach ridges as complementary sedimentary archives for the reconstruction of Holocene relative sea-level changes. Terra Nova **28**(1), 43–49. *https://doi.org/10.1111/ter.12187*

Shukla, P. *et al*. 2022: Summary for policymakers. In Shukla, P. *et al*. (eds): Climate change 2022: mitigation of climate change. Contribution of working group iii to the sixth assessment report of the intergovernmental panel on climate change. Cambridge: Cambridge University Press, 112 pp.

Skovborg, H. 1957: Vestersøs klægbanker mellem lemvig og harboøre er nu under plov. Hedeselskabets Tidsskrift **78**, 4.

Tamura, T., Murakami, F., Nanayama, F., Watanabe, K. & Saito, Y. 2008: Ground-penetrating radar profiles of Holocene raised-beach deposits in the Kujukuri strand plain, Pacific coast of eastern Japan. Marine Geology **248**(1), 11–27. *https://doi.org/10.1016/j.margeo.2007.10.002*

Vandenberghe, D., De Corte, F., Buylaert, J.-P. & Kučera, J. 2008: On the internal radioactivity in quartz. Radiation Measurements **43**(2–6), 771–775. *https://doi.org/10.1016/j.radmeas.2008.01.016*